A&A 623, A65 (2019)
https://doi.org/10.1051/0004-6361/201834748

Astronomy & Astrophysics

Globular clusters in the outer halo of M 31*

Song Wang[1], Jun Ma[1,2], and Jifeng Liu[1,2,3]

[1] Key Laboratory of Optical Astronomy, National Astronomical Observatories, Chinese Academy of Sciences, Beijing 100101, PR China
e-mail: songw@bao.ac.cn
[2] College of Astronomy and Space Sciences, University of Chinese Academy of Sciences, Beijing 100049, PR China
[3] WHU-NAOC Joint Center for Astronomy, Wuhan University, Wuhan, Hubei 430072, PR China

Received 30 November 2018 / Accepted 29 January 2019

ABSTRACT

In this paper, we present photometry of 53 globular clusters (GCs) in the M 31 outer halo, including the GALEX far-ultraviolet (FUV) and near-ultraviolet (NUV), SDSS *ugriz*, 15 intermediate-band filters of BATC, and 2MASS JHK_s bands. By comparing the multicolour photometry with stellar population synthesis models, we determine the metallicities, ages, and masses for these GCs, aiming to probe the merging/accretion history of M 31. We find no clear trend of metallicity and mass with the de-projected radius. The halo GCs younger than ∼8 Gyr are mostly located at the de-projected radii around 100 kpc, but this may be due to a selection effect. We also find that the halo GCs have consistent metallicities with their spatially associated substructures, which provides further evidence of the physical association between them. Both the disc and halo GCs in M 31 show a bimodal luminosity distribution. However, we should emphasise that there are more faint halo GCs which are not seen in the disc. The bimodal luminosity function of the halo GCs may reflect a different origin or evolution environment in their original hosts. The M 31 halo GCs include one intermediate metallicity group ($-1.5 < [Fe/H] < -0.4$) and one metal-poor group ($[Fe/H] < -1.5$), while the disc GCs have one metal-rich group more. There are considerable differences between the halo GCs in M 31 and the Milky Way (MW). The total number of GCs in M 31 is approximately three times greater than in the MW, however M 31 has about six times more halo GCs than the MW. Compared to the halo GCs of M 31, those of the MW are mostly metal-poor. Both the numerous halo GCs and the higher-metallicity component are suggestive of an active merger history of M 31.

Key words. galaxies: individual: M 31 – globular clusters: general – galaxies: stellar content

1. Introduction

The formation and evolution histories of galaxies are not quiescent. In hierarchical cosmological models (White & Rees 1978), galaxies grow in mass through continual interaction with nearby smaller satellites. Due to the process of phase mixing and the faint feature of the debris however, it is not simple for us to probe the merger/accretion events that occurred in the distant past. Generally, there are two ways to study the interaction history of galaxies. The first is by modelling galaxy interactions to reproduce the substructures discovered in the outskirts of the galaxy. Another way is to study the kinematics and stellar populations (e.g. metallicity, age) of the halo components.

Globular clusters (GCs) in the halos of galaxies are often considered to be the debris of their interaction history. Thus, they are valuable targets for studying the latter. In the Milky Way (MW), it has long been noticed that some GCs are deposited into the halo (e.g. Ibata et al. 1994; Da Costa & Armandroff 1995; Martin et al. 2004) by disrupting dwarfs (e.g. Sagittarius, Canis Major), although the Canis Major overdensity may also be produced by the thin and thick disc and spiral arm populations of the MW rather than by a collision with a dwarf satellite galaxy (e.g. Mateu et al. 2009). Some of the surviving dwarf galaxies associated with the MW lie in a rotating planar structure (Metz et al. 2007), and many GCs in the Galactic halo share this planar alignment (Keller et al. 2012; Pawlowski et al. 2012). These directly confirm the basic theory of the hierarchical galaxy formation model (McConnachie et al. 2009), and it is important to ascertain whether this assembly mode is prevalent in other galaxies.

An attractive alternative is our nearest large neighbour, the Andromeda Galaxy (M 31), which includes more GCs than the MW system (by a factor ≈3). Some surveys have discovered many substructures in the halo of M 31 (see Ferguson et al. 2002; Ibata et al. 2007; McConnachie et al. 2009, 2018, for details). Recently, the Pan-Andromeda Archaeological Survey (PAndAS) confirmed numerous halo GCs (e.g. Huxor et al. 2014), and the halo GCs show a flat radial surface-density profile beyond the projected distance $R_p \approx 30$ kpc (Huxor et al. 2011). Many of them are spatially associated with halo substructures. Using Monte Carlo simulations, Mackey et al. (2010) argued the case for a genuine physical association between the halo GCs and multiple tidal debris streams. Detailed kinematics analysis also shows that the GCs with $R_p > 30$ kpc exhibit coherent rotation around the minor optical axis of M 31 (Veljanoski et al. 2014), which appears to be rotating in the same direction as some dwarf galaxies associated with M 31 (Ibata et al. 2013). All of these discoveries have been interpreted as evidence of an accretion process (Côté et al. 2000; Huxor et al. 2011). However, a major limitation of previous studies is the lack of a comparison of the stellar populations (e.g. age, metallicity) between halo GCs and these substructures, which may provide strong evidence for or against the physical association.

* Full Tables 1 and 2 are only available at the CDS via anonymous ftp to cdsarc.u-strasbg.fr (130.79.128.5) or via http://cdsarc.u-strasbg.fr/viz-bin/qcat?J/A+A/623/A65

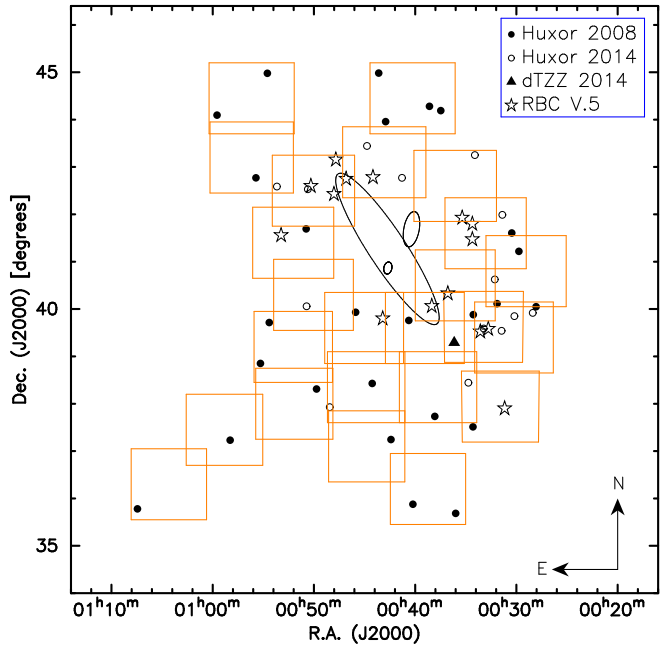

Fig. 1. Spatial distribution of 56 observed GCs. Each box represents a field view of 1.5° × 1.5°. The large ellipse has a semimajor axis of 2° (27 kpc), representing a disc with an inclination of 77.5° and a position angle of 38° (Kent 1989). The M 31 optical disc lies well within this ellipse. The two small ellipses are the D_{25} isophotes of NGC 205 (northwest) and M32 (southeast).

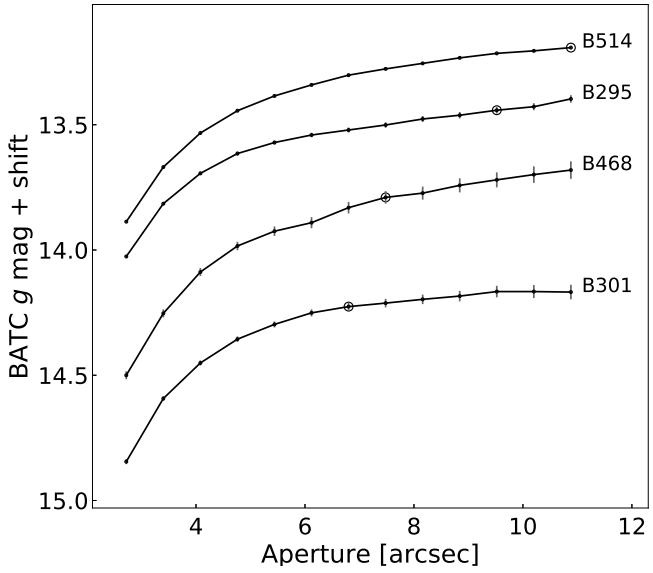

Fig. 2. Curve of growth using the BATC g-band photometry for several GCs as an example. The open circles represent the radii adopted for aperture photometry.

In this paper, we provide photometry of a set of GCs in the M 31 outer halo, using images obtained with the Beijing-Arizona-Taiwan-Connecticut (BATC) Multicolour Sky Survey Telescope. We construct observed spectral energy distributions (SEDs) from 1538 to 20 000 Å by combining the GALEX far-ultraviolet (FUV) and near-ultraviolet (NUV), SDSS *ugriz*, BATC, and Two Micron All Sky Survey (2MASS) near-infrared (NIR) data. Comparing the SEDs with simple stellar population (SSP) models, we estimate the metallicities, ages, and masses for the GCs. This paper is organised as follows. In Sect. 2, we present the BATC observations of the sample clusters and steps of relevant data processing and photometry. In Sect. 3, we derive the metallicities, ages, and masses of the sample clusters. In Sect. 4, we discuss the properties of the halo GCs by studying the association between them and halo substructures, and by comparing them with the M 31 disc GCs and Galactic halo GCs. Finally, we summarise our results in Sect. 5.

2. Sample, observations, and data reduction

2.1. Sample and BATC observations

We selected GCs in the outer halo of M 31, with projected distance $R_p > 20$ kpc, from Huxor et al. (2008, 2014), di Tullio Zinn & Zinn (2013, 2014), and the RBC V.5 catalogue (Galleti et al. 2004). Non-clusters were excluded with new classifications (Caldwell et al. 2009; Huxor et al. 2014). Although the cluster G339 was classified as "STAR" in Caldwell et al. (2009), the HST observation showed that it is a true GC (Barmby et al. 2007); we included it in our sample. This led to 113 outer halo GCs, of which 56 objects are located in the field of BATC observations (Fig. 1).

The BATC 60/90 cm Schmidt Telescope is at the Xinglong Station of the National Astronomical Observatories, Chinese Academy of Sciences (NAOC). The telescope includes 15 intermediate-band filters, covering a range of wavelengths from 3000 to 10 000 Å (see Fan et al. 1996, for details). The CCD size is 4k × 4k, with a resolution of 1.″36 pixel^{-1} (Fan et al. 2009).

2.2. BATC photometry

We processed all the CCD images with standard procedures including bias subtraction and flat fielding (Fan et al. 1996; Zheng et al. 1999). In order to improve the image quality, we combined multiple images of the same filter to one and performed photometry using the combined images. The BATC magnitudes were defined and obtained in a similar way as for the spectrophotometric AB magnitude system (e.g. Ma et al. 2009). We performed standard aperture photometry of our sample clusters using the PHOT routine in DAOPHOT (Stetson 1987). To ensure that we adopted the most appropriate photometric radius (R_{ap}) that includes all light from the object, we produced a curve of growth from the g-band photometry obtained through apertures with radii in the range of 2–8 pixels (≈2.7–10.9 arcsec) with increments of 0.5 pixels (Fig. 2). In order not to include the light from extraneous objects, we also checked the aperture radii carefully by visual examination of the images. This method ensures that we can correctly determine the total luminosities of clusters, especially as the use of small apertures for small clusters can maximise the signal-to-noise ratio (S/N) and minimise the contamination from nearby sources (Ma et al. 2015). The local sky background was measured in an annulus with an inner radius of R_{ap} + 2 pixels and a width of 5 pixels. Finding charts of the GCs and the final photometric radii are shown in Fig. 3.

Three clusters (HEC6, PAndAS-18, and PAndAS-40) are so faint that we cannot derive accurate photometry, and we removed them from the sample. The BATC photometry for the 53 GCs are listed in Table 1. For some objects, the magnitudes in some filters could not be obtained due to the low S/N. Magnitudes with an uncertainty larger than 0.3 were not used in subsequent SED fittings, although they are listed in Table 1.

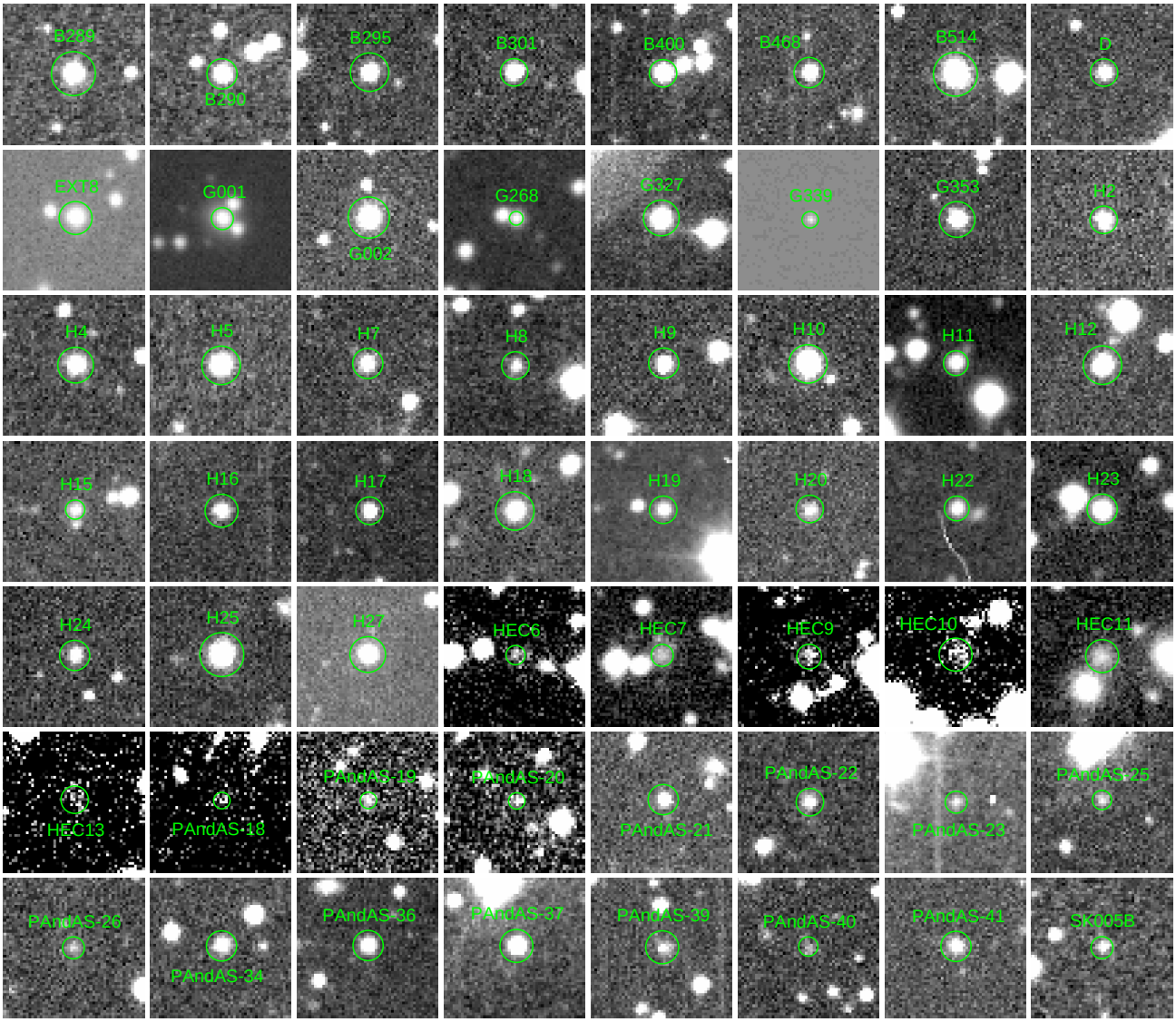

Fig. 3. Finding charts of 56 GCs in the BATC g band, obtained with the NAOC 60/90 cm Schmidt telescope. The field of view of each image is $\approx 2' \times 2'$. The green circles represent the radii for aperture photometry.

2.3. GALEX UV, SDSS, and 2MASS NIR photometry

Fitting SEDs with SSP models is a general way to determine the ages and masses for star clusters. Accurate and numerous photometric data can help derive accurate ages (de Grijs et al. 2003; Anders et al. 2004). The UV photometry is powerful for age estimation of young stellar populations, and the combination of UV photometry with optical observations enables one to break the age–metallicity degeneracy (Kaviraj et al. 2007; Fan & Wang 2017). Also, the age–metallicity degeneracy can be partially broken by adding NIR photometry to optical colours (de Jong 1996; Anders et al. 2004; Ma et al. 2009).

We downloaded the GALEX, SDSS, and 2MASS images and performed photometry using the same radii (in arcsec) following the BATC photometry. For some clusters, accurate photometric measurements cannot be obtained for some bands for various reasons. For example, G001 is saturated in the SDSS r-band observation and H19 is located on the asterism of one nearby star in the SDSS i- and z-band observations. To examine the quality and reliability of our photometry, we compared the aperture magnitudes of the 53 objects obtained here with previous results.

Kang et al. (2012) presented a catalogue of 700 confirmed star clusters in M 31, most of which are young disc clusters, and provided the most extensive and updated UV integrated photometry on the AB photometric system based on GALEX observations. Only a few clusters in their catalogue are found in our sample; the agreement between our NUV photometry and theirs is good (Fig. 4). Peacock et al. (2010) performed *ugriz* photometry for 1595 M 31 clusters and cluster candidates, using the drift scan images of M 31 obtained by the SDSS 2.5 m telescope. Huxor et al. (2014) reported the discovery of 59 halo GCs in M 31 from the PAndAS and determined the g and i magnitudes for them. The photometry from Peacock et al. (2010) are consistent with our results, but the magnitudes from Huxor et al. (2014) are systematically smaller than ours (Fig. 5). This is not surprising since Huxor et al. (2014) used larger radii (compared to ours) for aperture photometry.

We listed the GALEX UV, SDSS *ugriz*, and 2MASS NIR photometry of the sample GCs in Table 2. The SDSS and 2MASS magnitudes have been transferred to AB magnitudes. In addition, the magnitudes with an uncertainty larger than 0.3 were not used in subsequent analyses.

Table 1. BATC intermediate-band photometry of 53 sample GCs in M 31.

Object	*a*	*b*	*c*	*d*	*e*	*f*	*g*	*h*	*i*	*j*	*k*	*m*	*n*	*o*	*p*	R_{ap}
	(mag)	(mag)	(mag)	(mag)	(mag)	(mag)	(mag)	(mag)	(mag)	(mag)	(mag)	(mag)	(mag)	(mag)	(mag)	($''$)
(1)	(2)	(3)	(4)	(5)	(6)	(7)	(8)	(9)	(10)	(11)	(12)	(13)	(14)	(15)	(16)	(17)
B289	17.96	17.12	16.72	16.45	16.34	16.15	15.95	15.89	15.71	15.66	15.68	15.56	15.54	15.33	15.45	10.9
	0.06	0.04	0.02	0.04	0.02	0.01	0.02	0.01	0.03	0.01	0.02	0.02	0.02	0.02	0.05	
B290	19.26	18.74	18.05	17.76	17.44	17.24	17.0	16.88	16.65	16.61	16.57	16.46	16.4	16.15	16.23	7.5
	0.12	0.06	0.03	0.05	0.02	0.02	0.03	0.02	0.03	0.02	0.02	0.03	0.02	0.03	0.07	
B295	18.36	17.59	17.49	16.92	16.93	16.74	16.57	16.45	16.33	16.29	16.24	16.18	16.16	16.06	15.83	9.5
	0.07	0.04	0.03	0.03	0.02	0.02	0.01	0.01	0.01	0.01	0.02	0.03	0.02	0.02	0.07	
B301	19.4	18.8	18.26	17.55	17.44	17.27	16.99	16.85	16.66	16.6	16.42	16.39	16.27	16.24	16.15	6.8
	0.13	0.05	0.04	0.03	0.02	0.01	0.02	0.01	0.03	0.02	0.02	0.03	0.03	0.04	0.18	
B400	19.03	17.89	17.43	17.13	16.78	16.57	16.27	16.21	16.08	16.04	15.81	15.79	15.75	15.78	15.79	6.8
	0.08	0.04	0.03	0.01	0.02	0.02	0.03	0.02	0.02	0.02	0.02	0.01	0.02	0.02	0.04	
B468	...	19.23	18.87	18.42	18.34	18.12	17.78	17.63	17.52	17.44	17.03	17.28	17.16	17.32	16.58	7.5
	...	0.07	0.05	0.04	0.02	0.03	0.03	0.03	0.04	0.04	0.04	0.04	0.06	0.06	0.17	
B514	17.77	16.71	16.54	16.28	16.09	15.9	15.68	15.59	15.48	15.36	15.28	15.23	15.17	15.15	14.74	10.9
	0.07	0.06	0.06	0.01	0.02	0.03	0.03	0.01	0.02	0.01	0.03	0.03	0.04	0.03	0.05	
SDSS-D	19.59	18.93	18.5	17.94	17.85	17.71	17.47	17.37	17.22	17.16	17.05	16.96	16.93	17.1	16.5	6.8
	0.16	0.05	0.04	0.03	0.02	0.01	0.03	0.02	0.03	0.02	0.03	0.04	0.04	0.06	0.15	
EXT8	17.01	16.23	16.31	15.97	15.89	15.68	15.5	15.38	15.29	15.33	15.0	15.02	15.08	15.0	15.13	8.2
	0.05	0.03	0.02	0.04	0.04	0.02	0.02	0.02	0.02	0.02	0.01	0.01	0.01	0.04	0.03	
G001	15.98	15.38	15.01	14.19	14.18	14.01	13.71	13.64	13.42	13.36	13.23	13.37	13.13	13.18	13.04	5.4
	0.01	0.05	0.03	0.01	0.01	0.01	0.01	0.01	0.02	0.03	0.01	0.07	0.02	0.01	0.02	

Notes. Column 1 gives the GC names. Columns 2–16 present the magnitudes in the 15 BATC passbands. The 1σ magnitude uncertainties from DAOPHOT are listed for each object on the second line for corresponding passbands. Column 17 is the photometric apertures adopted in this paper. This table is available in its entirety in machine-readable form at the CDS.

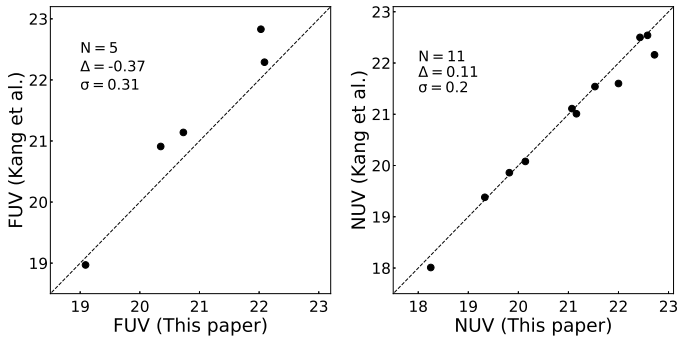

Fig. 4. Comparison of GALEX FUV (*left panel*) and NUV (*right panel*) photometry between Kang et al. (2012) and this paper.

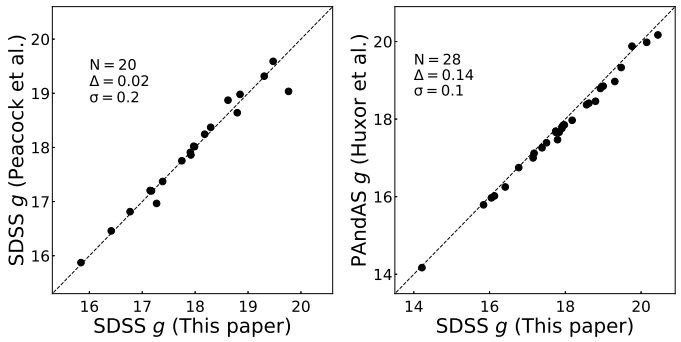

Fig. 5. Comparison of *g*-band photometry between Peacock et al. (2010; *left panel*), Huxor et al. (2014; *right panel*), and this paper.

2.4. Reddening and initial metallicities

To robustly and accurately estimate the ages and masses of our sample GCs, we first determined reddening and metallicities. For GCs in the outer halo, additional internal M 31 reddening towards these objects is likely to be negligible (Huxor et al. 2014). Therefore, we used the foreground colour excess $E(B-V)$ derived from Schlafly & Finkbeiner (2011) as the reddening value of the sample GCs.

Empirically nearly linear relations between different colours and metallicities have been well studied (e.g. Barmby et al. 2000; Peng et al. 2006; Fan et al. 2010b; Peacock et al. 2011; Harris et al. 2017). Using the photometry of M 31 GCs, Fan et al. (2010b) presented the correlations between the spectroscopic metallicities and 78 BATC colours. These colours can be used to estimate metallicities of our sample clusters. For most GCs, we used the colour $(f-o)_0$ – one of the most metal-sensitive colours – to estimate the metallicities. For H8 and HEC9, we used the colour $(f-k)_0$ because we cannot derive accurate *o*-band photometry for these two clusters. The metallicities will be input as an initial value in the following SED fitting.

3. Metallicity, age, and mass determination

3.1. Stellar populations and synthetic photometry

In order to determine the metallicities, ages, and masses of the sample GCs, we compared their SEDs with theoretical stellar population synthesis models. We adopted the (Bruzual & Charlot 2003, hereafter BC03) SSP models, which are based on the Padova isochrones (Bertelli et al. 1994) and the Salpeter (1955) stellar initial mass function. The full set of models span the wavelength range from 91 Å to 160 μm. These models cover ages from 0.1 Myr to 20 Gyr, and include six initial metallicities, Z = 0.00001, 0.0004, 0.004, 0.008, 0.02 (solar metallicity), and 0.05, corresponding to [Fe/H] = −2.25, −1.65, −0.64, −0.33, 0.09, and 0.56.

Table 2. GALEX, SDSS, and 2MASS NIR photometry of 53 sample GCs in M 31.

Object	FUV	NUV	u	g	r	i	z	J	H	K_s
	(mag)	(mag)	(mag)	(mag)	(mag)	(mag)	(mag)	(mag)	(mag)	(mag)
(1)	(2)	(3)	(4)	(5)	(6)	(7)	(8)	(9)	(10)	(11)
B289	20.73	19.82	...	...	...	...	...	15.19	15.24	15.88
	0.05	0.02	...	...	...	...	...	0.04	0.05	0.09
B290	23.81	22.43	...	...	...	...	...	16.09	15.9	15.9
	0.34	0.1	...	...	...	...	...	0.06	0.06	0.06
B295	21.38	20.44	18.25	16.96	16.44	16.16	15.99	15.79	15.99	16.52
	0.11	0.01	0.04	0.01	0.01	0.01	0.03	0.06	0.08	0.14
B301	23.3	22.14	19.18	17.54	16.82	16.49	16.24	15.94	15.57	15.97
	0.24	0.04	0.06	0.02	0.01	0.01	0.02	0.05	0.05	0.07
B400	22.45	21.16	18.54	16.89	16.24	15.88	15.74	15.41	15.38	15.56
	0.17	0.05	0.04	0.01	0.01	0.01	0.02	0.03	0.04	0.05
B468	23.26	22.88	19.85	18.3	17.69	17.36	17.23	17.17	16.88	16.25
	0.33	0.2	0.11	0.03	0.02	0.02	0.06	0.14	0.13	0.1
B514	20.61	19.54	17.73	16.13	15.54	15.25	15.13	15.08	14.68	15.47
	0.06	0.03	0.03	0.01	0.01	0.01	0.01	0.04	0.04	0.07
SDSS-D	...	20.55	19.29	17.9	17.34	17.03	17.03	17.06	16.66	17.27
	...	0.09	0.07	0.02	0.02	0.02	0.04	0.11	0.1	0.18
EXT8	...	18.69	16.99	15.84	15.51	15.15	14.97	14.89	14.84	15.46
	...	0.06	0.02	0.01	0.01	0.01	0.01	0.02	0.03	0.05
G001	19.09	18.25	16.04	14.22	...	13.26	13.04	12.71	12.51	12.85
	0.02	0.01	0.01	0.01	...	0.01	0.01	0.01	0.01	0.01

Notes. Column 1 gives the GC names. Columns 2–11 present the magnitudes from GALEX, SDSS, and 2MASS NIR observations. All magnitudes are in the AB magnitude system. The 1σ magnitude uncertainties from DAOPHOT are listed for each object on the second line for the corresponding passbands. This table is available in its entirety in machine-readable form at the CDS.

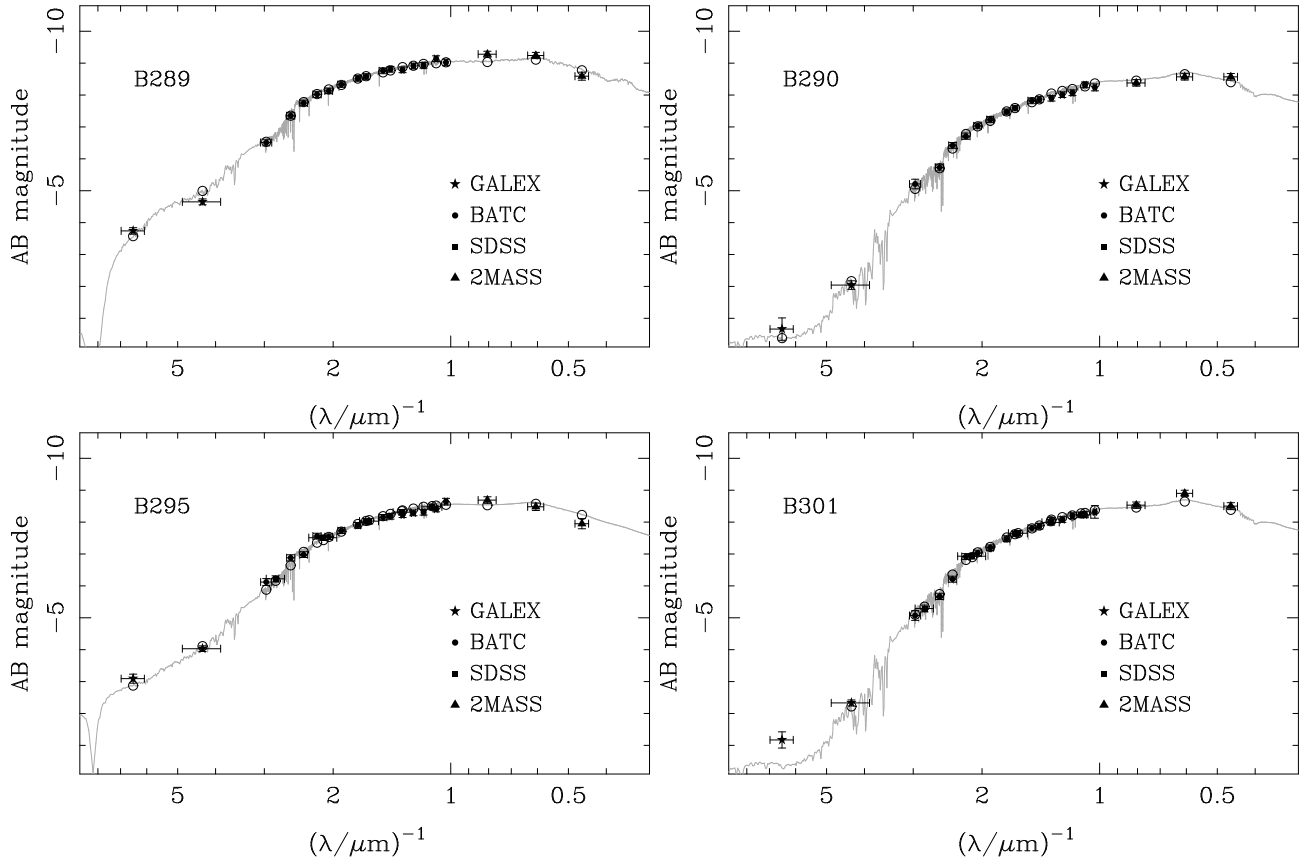

Fig. 6. Best-fitting integrated SEDs of the BC03 SSP models and the intrinsic SEDs for several example GCs. The filled symbols represent photometric data points, while the open circles represent the calculated magnitudes of the model SEDs for each filter.

Table 3. Reddening values, metallicities, ages, and masses of 53 sample GCs in M 31.

Object	$E(B-V)$	[Fe/H]	Age (Gyr)	Mass ($10^4\,M_\odot$)
(1)	(2)	(3)	(4)	(5)
B289	0.07	−1.1 ± 0.1	2.0 ± 0.2	24.7 ± 0.7
B290	0.06	−0.4 ± 0.1	6.7 ± 0.8	27.8 ± 0.9
B295	0.05	−1.9 ± 0.1	14	46 ± 2
B301	0.05	−0.4 ± 0.1	8 ± 1	36 ± 1
B400	0.08	−1.3 ± 0.1	14	80 ± 2
B468	0.06	−1.1 ± 0.1	14	25 ± 2
B514	0.05	−1.7 ± 0.1	14	117 ± 3
SDSS-D	0.05	−2.2 ± 0.1	14	21 ± 1
EXT8	0.06	−2.0 ± 0.1	3.4 ± 0.6	51.9 ± 0.9
G001	0.05	−1.1 ± 0.1	14	961 ± 3
G002	0.05	−1.8 ± 0.1	14	131 ± 3
G268	0.07	−0.8 ± 0.1	14	68 ± 1
G327	0.07	−1.2 ± 0.1	14	129 ± 2
G339	0.08	−1.4 ± 0.1	14	31 ± 1
G353	0.07	−1.9 ± 0.1	14	24 ± 2
H2	0.05	−2.2 ± 0.1	13 ± 3	27 ± 2
H4	0.06	−1.2 ± 0.1	14	40 ± 2
H5	0.07	−1.3 ± 0.1	2.0 ± 0.2	20.1 ± 0.8
H7	0.05	−2.1 ± 0.1	14	9.6 ± 0.7
H8	0.05	−0.5 ± 0.2	9 ± 4	…
H9	0.05	−1.0 ± 0.1	1.3 ± 0.2	4.0 ± 0.3
H10	0.06	−1.5 ± 0.1	14	102 ± 2
H11	0.06	−2.2 ± 0.1	14	41 ± 2
H12	0.06	−1.2 ± 0.1	2.2 ± 0.2	16.7 ± 0.8
H15	0.05	−1.3 ± 0.1	4 ± 1	3.5 ± 0.4
H16	0.07	−1.5 ± 0.1	14	29 ± 2
H17	0.04	−1.5 ± 0.1	14	24 ± 1
H18	0.08	−1.9 ± 0.1	14	60 ± 3
H19	0.05	−0.9 ± 0.1	1.3 ± 0.2	4.8 ± 0.3
H20	0.05	−1.2 ± 0.2	2.1 ± 0.3	…
H22	0.04	−1.9 ± 0.1	14	34 ± 2
H23	0.04	−1.4 ± 0.1	14	55 ± 2
H24	0.09	−1.2 ± 0.1	14	14 ± 1
H25	0.08	−1.3 ± 0.1	2.6 ± 0.3	13 ± 1
H27	0.05	−1.9 ± 0.1	14	54 ± 2
HEC7	0.08	−2.2 ± 0.1	14	4.3 ± 0.9
HEC9	0.05	−2.0 ± 0.5	14	…
HEC10	0.09	−1.4 ± 0.6	14	…
HEC11	0.04	−2.2 ± 0.1	14	8 ± 2
HEC13	0.04	−2.2 ± 0.6	14	…
PAndAS-19	0.05	−0.6 ± 0.3	3 ± 1	…
PAndAS-20	0.06	−0.2 ± 0.2	2.8 ± 0.6	…
PAndAS-21	0.05	−1.6 ± 0.1	9 ± 2	16 ± 1
PAndAS-22	0.06	−0.9 ± 0.1	5 ± 1	3.0 ± 0.5
PAndAS-23	0.05	−0.5 ± 0.2	7 ± 2	…
PAndAS-25	0.06	−2.0 ± 0.4	14	…
PAndAS-26	0.05	−0.9 ± 0.1	14	2.1 ± 0.4
PAndAS-34	0.06	−0.5 ± 0.1	6.4 ± 0.6	12.5 ± 0.9
PAndAS-36	0.06	−1.9 ± 0.1	14	33 ± 2
PAndAS-37	0.05	−0.4 ± 0.1	14	47 ± 2
PAndAS-39	0.08	−1.0 ± 0.2	6 ± 2	…
PAndAS-41	0.08	−1.5 ± 0.1	14	30 ± 2
SK005B	0.06	0.5 ± 0.1	13 ± 3	20.0 ± 0.9

We convolved the BC03 SSP models with the response curves of the GALEX FUV and NUV, SDSS *ugriz*, BATC, and 2MASS JHK_s filters to obtain synthetic UV, optical, and NIR photometry, for subsequent comparison with the observational integrated magnitudes. The synthetic ith filter magnitude in the AB magnitude system can be computed as

$$m_i = -2.5 \log \frac{\int_\nu F_\nu \varphi_i(\nu) \mathrm{d}\nu}{\int_\nu \varphi_i(\nu) \mathrm{d}\nu} - 48.60, \quad (1)$$

where F_ν is the theoretical SED and φ_i is the response curve of the ith filter of the corresponding photometric systems. Here, F_ν varies with age and metallicity.

3.2. Fittings

We used a χ^2 minimisation test to determine the SSP model that is most compatible with the observed SED, following

$$\chi^2 = \sum_{i=1}^{n} \frac{[m_{\nu_i}^{\mathrm{intr}} - m_{\nu_i}^{\mathrm{mod}}(t, Z)]^2}{\sigma_i^2}, \quad (2)$$

where $m_{\nu_i}^{\mathrm{intr}}$ represents the intrinsic integrated magnitude in the ith filter, $m_{\nu_i}^{\mathrm{mod}}(t, Z)$ is the integrated magnitude in the same filter of a theoretical SSP at age t and metallicity Z, and n is the number of the filters used for fitting. The uncertainty σ_i is calculated as

$$\sigma_i^2 = \sigma_{\mathrm{obs},i}^2 + \sigma_{\mathrm{mod},i}^2 + (R_{\lambda_i} * \sigma_{\mathrm{red}})^2 + \sigma_{\mathrm{md},i}^2, \quad (3)$$

which is a combination of the observational uncertainty $\sigma_{\mathrm{obs},i}$, the uncertainty associated with the model itself $\sigma_{\mathrm{mod},i}$, the uncertainty of the reddening value σ_{red}, and the uncertainty of the distance modulus $\sigma_{\mathrm{md},i}$. We adopted $\sigma_{\mathrm{mod},i} = 0.05$ mag for all the filters (Ma et al. 2007b, 2012; Wang et al. 2010). The R_{λ_i}, defined as $A_{\lambda_i}/E(B-V)$, was calculated following Cardelli et al. (1989). The $\sigma_{\mathrm{md},i}$ is always 0.07 mag from $(m-M)_0 = 24.47 \pm 0.07$ mag (McConnachie et al. 2005). During the fitting, the age and metallicity were free parameters, but the metallicity was constrained in the range (i.e. initial metallicity ± metallicity uncertainty) derived from the BATC colours (Sect. 2.4). The upper limit of age in the BC03 models is 20 Gyr, much older than that of the universe. Thus, we adopted a truncated age of 14 Gyr for clusters if their fitted ages are older than that (Fan et al. 2010a; Caldwell et al. 2011; Caldwell & Romanowsky 2016). The fitting results of the 53 GCs are listed in Table 3. As an example, we presented the results of fittings for some sample clusters in Fig. 6.

The comparison of input and fitted metallicities shows good agreement (Fig. 7). That means the metallicities deduced from the BATC colours are credible. One cluster (SK005B) has extremely high metallicity estimation ([Fe/H] > 0.5). The metallicities estimated from other BATC colours (e.g. $(f-k)_0$, $(h-k)_0$) are also higher than 0.5. We then estimated the metallicity from other optical and NIR colours (e.g. $(U-R)_0$, $(V-I)_0$, and $(V-K)_0$) using the relations from Barmby et al. (2000), and all the estimates are higher than 0.5. We suppose that the extinction of SK005B is underestimated. When we use $E(B-V) = 0.4$, the values of metallicity derived from the colours are from −1 to 0. However, when we fix the $E(B-V) = 0.4$ and re-do the SED fitting, the fitted metallicity is still higher than 0.5. This is unreasonable, and therefore we removed SK005B from the following analysis.

We determined the masses of the sample GCs sequentially. The BC03 SSP models are normalized to a total mass of 1 $M_\odot$ in stars at age $t = 0$; these models provide absolute magnitudes (in the Vega system) in *UBVRI* and 2MASS JHK_s filters. Therefore, the difference between the intrinsic and model absolute magnitudes provides a direct measurement of the cluster mass. For each GC, we estimated the masses using magnitudes in the JHK_s bands and averaged them as the final cluster mass. The masses of 13 clusters were not determined because their JHK_s magnitudes were not available here.

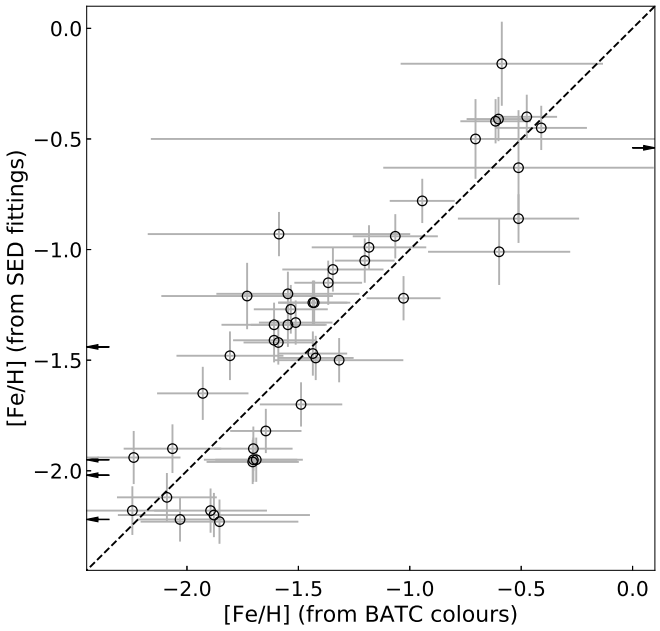

Fig. 7. Comparison of metallicities deduced from colours and SED fittings.

3.3. Comparison with previous determinations

In this paper, we determine the metallicities, ages, and masses for 53 GCs by comparing their multicolour photometries with theoretical SSP models. In Figs. 8–10, we compare our estimates with those in the literature: Fan et al. (2010a), Chen et al. (2016), and Caldwell et al. (2011), Caldwell & Romanowsky (2016).

Fan et al. (2010a) presented updated *UBVRI* photometry for 970 star clusters in M 31, and determined the metallicities, ages, and masses by comparing the integrated SEDs (*UBVRI*) with BC03 SSP models. Eleven of them are found in our sample. There is some discrepancy between our metallicity estimates and theirs, and their age and mass estimates are systematically smaller than ours. This is likely caused by the larger reddening values they used. Of these 11 shared clusters, the three with the largest $E(B-V)$ values from 0.2 to 0.5 (B289, G339, and G353) obtained from free fitting (Fan et al. 2010a) are also the youngest. Considering that the reddening, metallicity, and age are degenerate during the SED fitting, their fitting results may be inaccurate. Furthermore, our SEDs include the photometric data in many bands, especially in the *UV* bands, which can help derive accurate ages of star clusters (de Grijs et al. 2003; Anders et al. 2004).

Caldwell et al. (2011) estimated metallicities using the Lick <Fe> indices, and determined ages for clusters with [Fe/H] > −1 using the automatic stellar population analysis programme EZ_Ages. Caldwell & Romanowsky (2016) collected metallicities for a number of M 31 GCs from previous studies (e.g. Mackey et al. 2006, 2007; Colucci et al. 2014). Forty-three objects are in common between our sample and those of Caldwell et al. (2011), Caldwell & Romanowsky (2016). Both their metallicities and mass estimates are in agreement with ours. Caldwell et al. (2011), Caldwell & Romanowsky (2016) reported an age of 14 Gyr for all these clusters, since they simply assigned an age of 14 Gyr to all clusters with [Fe/H] < −0.95 dex, meaning that no precise age was determined. In our study, among these sources, 15 objects have ages younger than 14 Gyr (i.e. four objects have ages between 5 and 14 Gyr, and 11 objects have ages ranging from 1 to 5 Gyr).

Using the LAMOST spectra of M 31 star clusters, Chen et al. (2016) determined metallicities, ages, and masses from full spectral fitting with the PEGASE-HR models. Nineteen of them are included in our sample. For metallicity and mass, the agreement between our estimates and their estimates is generally good. The discrepancy between the age estimates is clear, but the uncertainties of the ages are quite large. Four clusters (B289, EXT8, H19, and H20) were estimated to be older than 10 Gyr in Chen et al. (2016), but younger than 4 Gyr (i.e. 2.0, 3.4, 1.3, and 2.1 Gyr) in our study. For H19, the photometry is too faint for accurate SED fitting. We checked the LAMOST observations of the four clusters, and found the S/Ns of all these spectra to be relatively low: the S/Ns range from 2 to 10 in the *g* band and from 3 to 17 in the *r* band. Therefore, the age estimates from spectral fitting may be inaccurate for these clusters.

We also collected metallicities from several other studies. Using the Keck/HIRES spectra, Alves-Brito et al. (2009) and Colucci et al. (2014) measured the metallicities for a small sample of M 31 GCs. Sakari et al. (2015) presented detailed chemical abundances for seven M 31 outer halo GCs, which were derived from the spectra taken with the Hobby-Eberly Telescope. Based on the HST observations, the metallicities for a group of M 31 GCs were measured with the colour-magnitude diagram (CMD) fitting (Rich et al. 2005; Mackey et al. 2006, 2007). Although the results from different methods may be discrepant, in general most of our estimates are consistent with those derived from high-resolution spectra or CMD fitting (Table 4).

4. Discussion

4.1. Spatial distribution

Using these halo GCs with homogeneously determined metallicities, ages, and masses, we can now investigate their spatial distribution. To derive the de-projected galactocentric distance, firstly we used an X, Y projection to refer to the relative positions of the objects (Huchra et al. 1991; Perrett et al. 2002). The X coordinate projects along the major axis of M 31, increasing towards the northeast; the Y coordinate extends along the minor axis of the M 31 disc, where positive Y increases towards the northwest. We adopted $\alpha_0 = 00^{\rm h}42^{\rm m}44\overset{\rm s}{.}30$ and $\delta_0 = +41°16'09\overset{''}{.}0$ (J2000.0) as the centre of M 31, and used a position angle of PA = 38° for the major axis (Kent 1989). Formally,

$$X = A\sin(\mathrm{PA}) + B\cos(\mathrm{PA}) \quad \text{and}$$
$$Y = -A\cos(\mathrm{PA}) + B\sin(\mathrm{PA}), \tag{4}$$

where $A = \sin(\alpha - \alpha_0)\cos\delta$ and $B = \sin\delta\cos\delta_0 - \cos(\alpha - \alpha_0)\cos\delta\sin\delta_0$. Subsequently, using an inclination angle of IA = 77.5° for the disc of M 31, we calculated the de-projected radius as $\sqrt{X^2 + (Y/\cos(\mathrm{IA}))^2}$.

Figure 11 shows the metallicity, ages, and masses of the sample clusters as a function of de-projected radius. The metallicity shows no clear relation with the de-projected galactocentric distance within 200 kpc. Most of the GCs (51 out of 53) have metallicities lower than −0.4, and can be divided into one intermediate-metallicity group and one metal-poor group (Caldwell & Romanowsky 2016). The clusters younger than ~8 Gyr are mostly located at de-projected distances around 100 kpc, but this may be caused by a selection effect. Most GCs have masses between 10^4 and $10^6\,M_\odot$, except for the most massive cluster G001, which has a mass around $10^7\,M_\odot$. No clear relation is seen for the mass and de-projected distance.

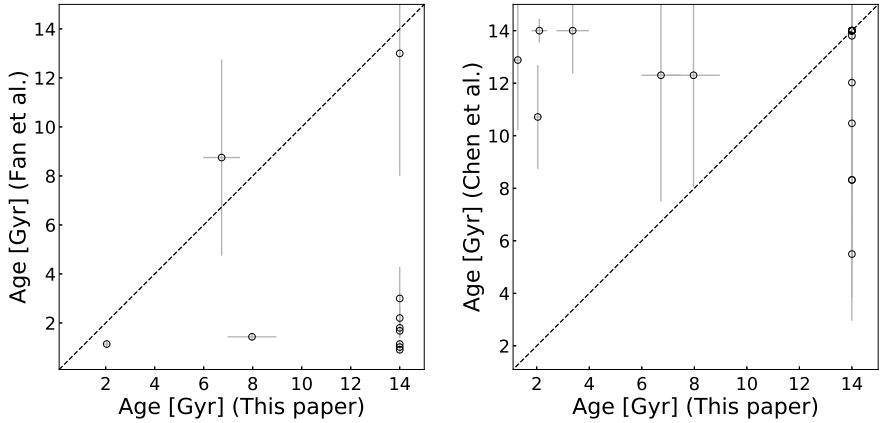

Fig. 8. Comparison of the ages obtained here with those obtained by previous works (from *left panel* to *right panel*): Fan et al. (2010a) and Chen et al. (2016). For clusters from Chen et al. (2016), we set their age estimates to 14 Gyr if they are older than that.

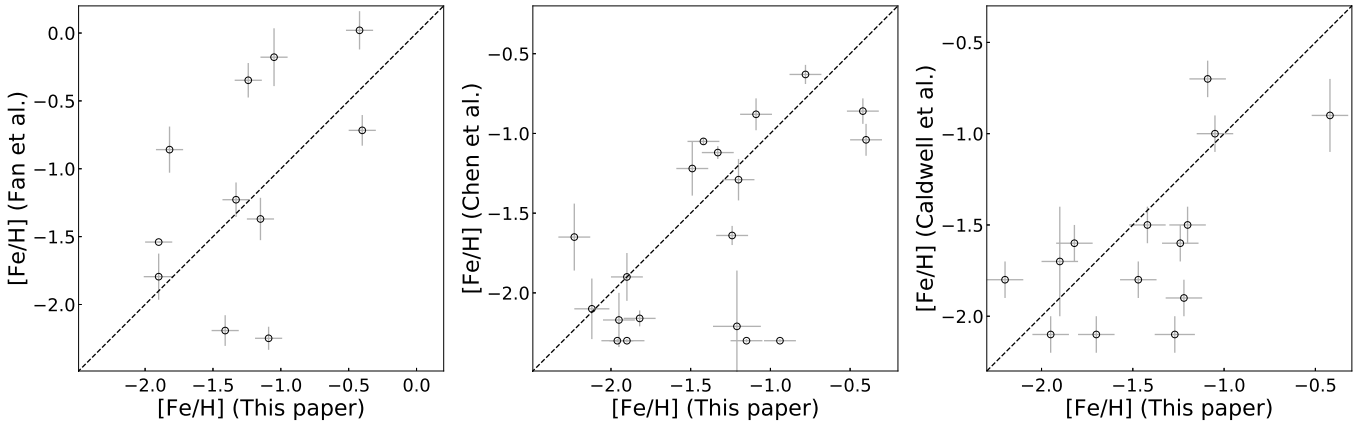

Fig. 9. Comparison of the metallicities obtained here with those obtained by previous works (from *left panel* to *right panel*): Fan et al. (2010a), Chen et al. (2016), and Caldwell et al. (2011), Caldwell & Romanowsky (2016).

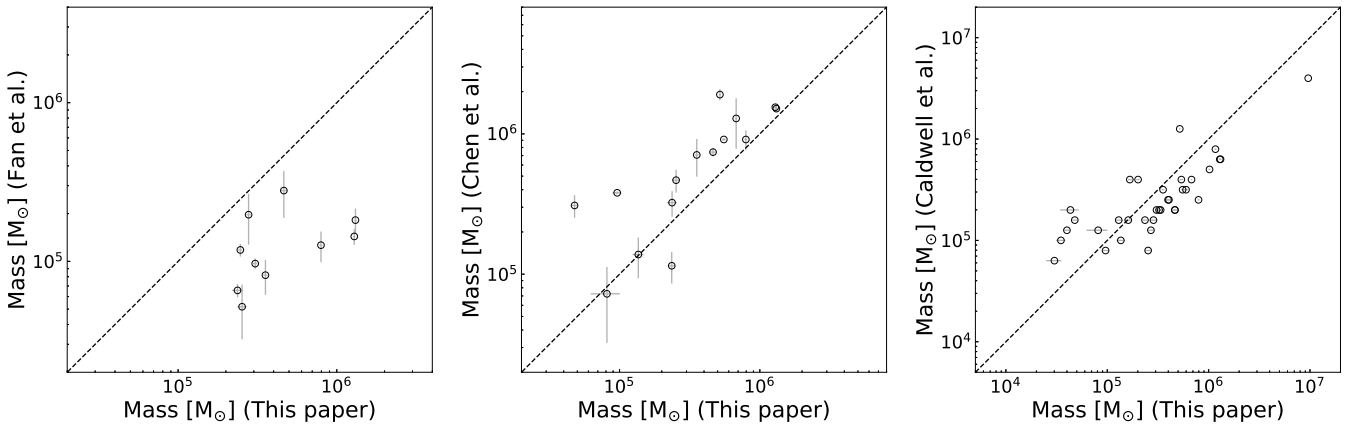

Fig. 10. Comparison of the masses obtained here with those obtained by previous works (from *left panel* to *right panel*): Fan et al. (2010a), Chen et al. (2016), and Caldwell et al. (2011), Caldwell & Romanowsky (2016).

We divided our sample GCs into different groups using [Fe/H] and age, and studied the spatial distribution of each group (Fig. 12). There are some clear features: (1) All GCs younger than 3 Gyr have metallicities [Fe/H] > -1.5, and most of them are located in the southwest region; (2) most GCs (18 out of 21) with [Fe/H] < -1.5 have an age of 14 Gyr; and (3) there is an extended feature along the direction of M 31 minor optical axis and towards M 33 for GCs with [Fe/H] < -1.5 that consists of four GCs (i.e., H22, H27, HEC11, and HEC13), spanning up to 60 kpc. This latter suggests a possible interaction between M 31 and M 33 in the past; however, the feature is likely caused by our unevenly pointed observations (see Fig. 1).

4.2. Association with substructures

The spatial distribution of halo GCs in M 31 is anisotropical. Spatial density maps display a striking association between many GCs and the most luminous substructures in the

Table 4. Metallicities for GCs measured from this paper and previous studies.

Object	[Fe/H]									
	This paper	F10	Ch17	A09	Ca11	S15	R05	M06	M07	Co14
(1)	(2)	(3)	(4)	(5)	(6)	(7)	(8)	(9)	(10)	(11)
B289	−1.1 ± 0.1	−1.37 ± 0.16	−2.30 ± 0.01	...	...	...	...	...	...	...
B290	−0.4 ± 0.1	−0.72 ± 0.11	−1.04 ± 0.10	...	...	...	...	...	...	...
B295	−1.9 ± 0.1	−1.54 ± 0.00	−1.90 ± 0.15	...	−1.7 ± 0.3	...	...	...	...	...
B301	−0.4 ± 0.1	0.02 ± 0.14	−0.86 ± 0.08	...	−0.9 ± 0.2	...	...	...	...	...
B400	−1.3 ± 0.1	−1.23 ± 0.13	−1.12 ± 0.04	...	...	...	...	...	...	...
B468	−1.1 ± 0.1	−2.25 ± 0.09	−0.88 ± 0.10	...	...	...	−0.7	...	...	...
B514	−1.7 ± 0.1	...	...	...	...	...	...	...	−2.14	−1.74
EXT8	−2.0 ± 0.1	...	−2.30 ± 0.01	...	...	...	...	...	...	...
G001	−1.1 ± 0.1	−0.18 ± 0.21	...	...	...	...	−1.0	...	...	...
G002	−1.8 ± 0.1	−0.86 ± 0.17	−2.16 ± 0.05	...	...	...	...	...	...	−1.63
G268	−0.8 ± 0.1	...	−0.63 ± 0.06	...	...	...	...	...	...	...
G327	−1.2 ± 0.1	−0.35 ± 0.13	−1.64 ± 0.06	...	...	...	...	...	...	−1.65
G339	−1.4 ± 0.1	−2.19 ± 0.11	...	...	...	...	...	...	...	...
G353	−1.9 ± 0.1	−1.79 ± 0.17	−2.30 ± 0.01	...	...	...	...	...	...	...
H4	−1.2 ± 0.1	...	...	...	...	...	...	...	−1.94	...
H5	−1.3 ± 0.1	...	...	...	...	...	...	...	−2.14	...
H7	−2.1 ± 0.1	...	−2.10 ± 0.19	...	...	...	...	...	...	...
H10	−1.5 ± 0.1	...	...	−1.40 ± 0.10	...	−1.36 ± 0.02	...	...	−1.84	−1.45
H17	−1.5 ± 0.1	...	−1.22 ± 0.17	...	...	...	...	...	...	...
H19	−0.9 ± 0.1	...	−2.30 ± 0.01	...	...	...	...	...	...	...
H20	−1.2 ± 0.2	...	−2.21 ± 0.35	...	...	...	...	...	...	...
H23	−1.4 ± 0.1	...	−1.05 ± 0.02	...	...	−1.12 ± 0.02	...	...	−1.54	...
H24	−1.2 ± 0.1	...	−1.29 ± 0.13	...	...	...	...	...	−1.54	...
H27	−1.9 ± 0.1	...	−2.17 ± 0.17	−1.73 ± 0.10	...	...	...	...	−2.14	...
HEC7	−2.2 ± 0.1	...	...	...	...	...	...	−1.84	...	...
HEC11	−2.2 ± 0.1	...	−1.65 ± 0.21	...	...	...	...	...	...	...

Notes. References for metallicities in previous studies: R05 – Rich et al. (2005); M06 – Mackey et al. (2006); M07 – Mackey et al. (2007); A09 – Alves-Brito et al. (2009); F10 – Fan et al. (2010a); Ca11 – Caldwell et al. (2011); Co14 – Colucci et al. (2014); S15 – Sakari et al. (2015); Ch16 – Chen et al. (2016).

Table 5. Metallicities of the GCs and their specially associated substructures.

Substructures		GC	
Name	[Fe/H] range	Name	[Fe/H]
(1)	(2)	(3)	(4)
Stream C	[−2.5, 0][a]	HEC13	−2.2±0.6
Stream D	[−2.5, −1.1][b]	HEC11	−2.2±0.1
		H23	−1.4±0.1
		H24	−1.2±0.1
		PAndAS-41	−1.5±0.1
Giant Stream	[−2.5, 0][a]	H19	−0.9±0.1
		H22	−1.9±0.1
		PAndAS-37	−0.4±0.1

Notes. [(a)][Fe/H] range is from Ibata et al. (2014). [(b)][Fe/H] range is from Mackey et al. (2018).

metal-poor field halo (Mackey et al. 2018). Kinematic analysis suggests a dynamical link between the halo GCs and the substructures (i.e. streams or overdensities) that they project onto (Veljanoski et al. 2014). On the other hand, many of the surviving dwarf galaxies associated with M 31 lie in a thin rotating planar structure (Ibata et al. 2013), and the outer halo GC system appears to be rotating in the same direction as the dwarfs, although with a different rotation axis (Veljanoski et al. 2014). All of these indicate that a number of outer halo GCs in M 31 were accreted from their parent dwarf galaxies. Recently, Mackey et al. (2018) reported that about 35–60% of remote clusters were accreted into the outskirts of M 31 at late times with their parent dwarfs, while more than 40% of the clusters were accumulated at early times from disrupted primitive satellites. This suggests that the M 31 halo system ($R_p \geq 25$ kpc) accreted GCs from external galaxies over a Hubble time (see Mackey et al. 2018, for details).

To investigate these in more detail, we collected the discovered stellar substructures from previous studies: the four minor-axis tangent streams A–D (Ibata et al. 2007); the giant stream (Ibata et al. 2001); the northeast structure (Zucker et al. 2004; Ibata et al. 2005); the northwest stream (McConnachie et al. 2009); and the southwest cloud (McConnachie et al. 2009). We collected the contours of these substructures from Fig. 3 of Mackey et al. (2010). There are about 30 GCs in total (including 8 GCs in our sample) showing spatial coincidence with these halo substructures (Fig. 13).

We collected the metallicities of substructures from previous studies (Ibata et al. 2005, 2007, 2014; Mackey et al. 2018). The stream C, giant stream, and northeast structure have a wider range of metallicites than other substructures (Mackey et al. 2018). The metallicities of GCs show good agreement with those of their specially associated substructures (Table 5). The metallicity consistency indicates that they have similar stellar

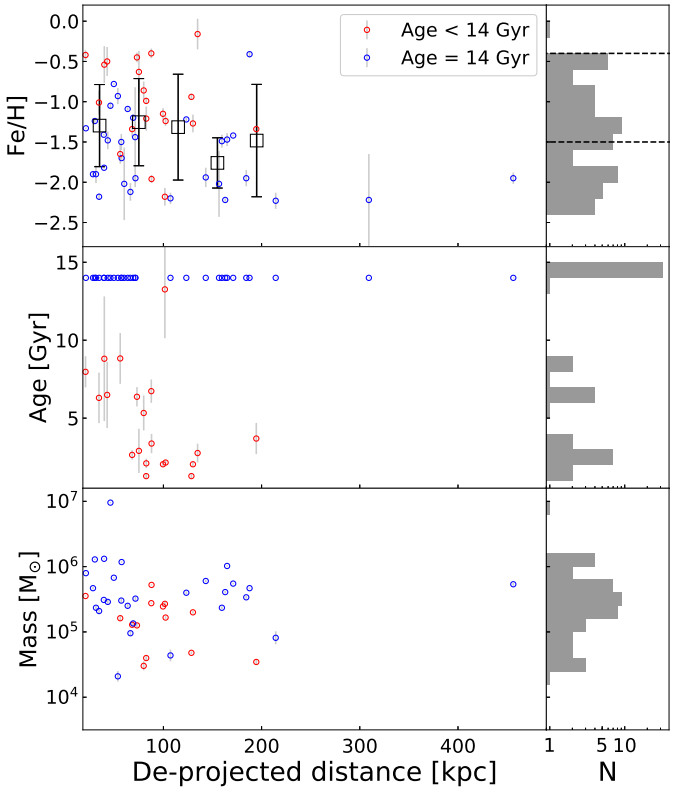

Fig. 11. *Top panel*: distribution of [Fe/H] of GCs against de-projected radius. The red and blue circles represent the GCs younger and older than 14 Gyr, respectively. The squares represent the mean metallicity values in different de-projected galactocentric distance for the GCs. The two dashed lines represent metallicities [Fe/H] = −0.4 and [Fe/H] = −1.5. *Middle panel*: age vs. de-projected radius. *Bottom panel*: mass vs. de-projected radius.

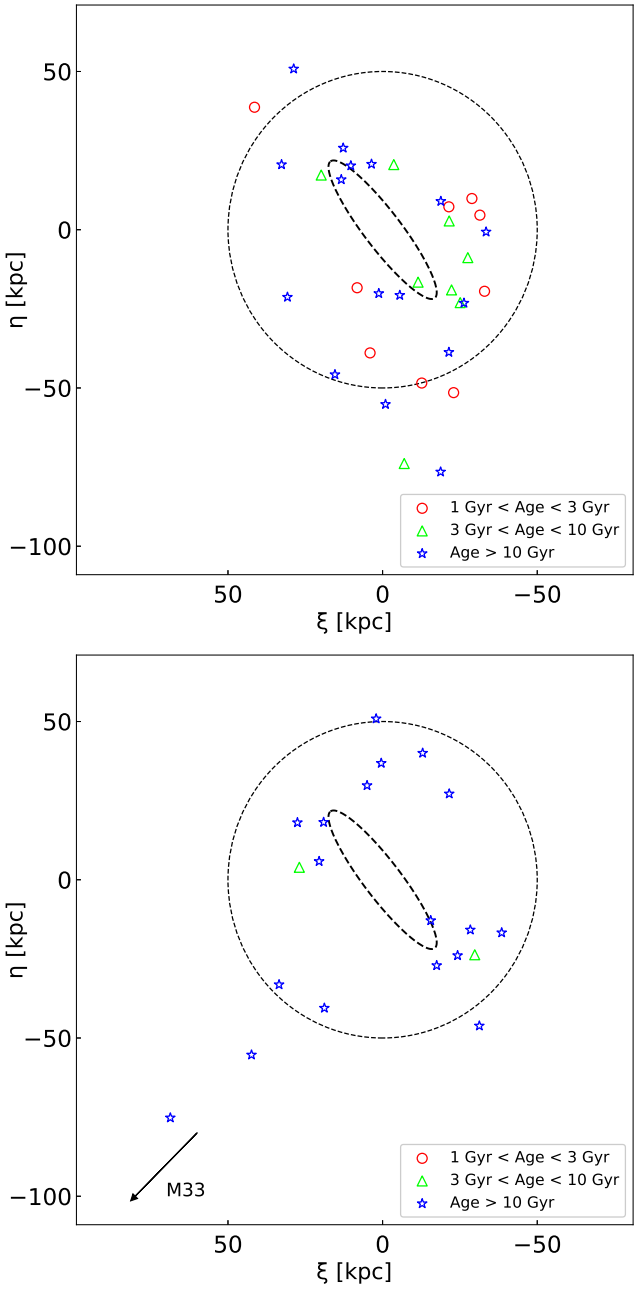

Fig. 12. *Top panel*: spatial distribution of GCs with [Fe/H] > −1.5. The dashed ellipse has a semimajor axis of 2° (27 kpc) representing a disc, while the dashed circle lies at a radius of 50 kpc. *Bottom panel*: spatial distribution of GCs with [Fe/H] < −1.5.

populations, which adds further support to the physical association between them.

4.3. Comparison with M 31 disc GC system

The GC luminosity function (GCLF) – the brightness distribution of GCs in a galaxy, can be used to constrain the possibilities for GC formation and destruction (see Nantais et al. 2006, and references therein). We determined the GCLFs for M 31 halo and disc GCs respectively, using the BATC g-band and 2MASS J-band magnitudes. We collected 358 disc GCs from Caldwell et al. (2011), Caldwell & Romanowsky (2016) with $R_p \leq 20$ kpc, of which 296 have BATC g magnitudes (Ma et al. 2015) and 329 have 2MASS J magnitudes (Wang et al. 2014). For the halo GCs in our study, 53 and 44 have BATC g and 2MASS J magnitude estimates, respectively.

We fitted both the GCLFs using both a single-Gaussian function and a double-Gaussian function (Table 6), and plotted the results in Fig. 14. For the disc GCs, the F-test shows that the double Gaussian fitting is statistically significantly better than the single-Gaussian fitting. The halo GCs show significant bimodality with the BATC g magnitudes, with the probability of the F-test being less than 2%. It is striking that there are many more faint GCs in the halo ($M_g > -6$) than in the disc, and these faint GCs contribute to the fainter part in the halo GCLF. Mackey et al. (2010) argued that perhaps up to ~80% of the GCs in the M 31 outer halo were accreted from their parent dwarf galaxies. Therefore, this bimodality of the GCLF may reflect a different origin or evolution environment for these halo GCs in their hosts (see Huxor et al. 2014; Mackey et al. 2018, for details).

Previous studies show a bimodal distribution of metallicity of M 31 GCs (e.g. Perrett et al. 2002; Puzia et al. 2005; Fan et al. 2008). However, Caldwell et al. (2011), Caldwell & Romanowsky (2016) argued that the bimodal metallicity distribution is due to the contamination of young disc clusters, and the M 31 distribution can be divided into three major metallicity groups based on their radial distributions. Figure 15 shows the distributions of metallicity and mass for the outer-halo GCs and the disc GCs, respectively. Compared to the disc GCs, there are only two metallicity groups for the outer-halo GCs – one group with

Table 6. Fitting results of the luminosity functions of M 31 disc and halo GC systems.

GC	Double Gaussian				Single Gaussian		P^a
	μ_1	σ_1	μ_2	σ_2	μ	σ	
(1)	(2)	(3)	(4)	(5)	(6)	(7)	(8)
				BATC g			
Disc	-8.41 ± 0.05	0.96 ± 0.04	-8.91 ± 0.04	-0.26 ± 0.05	-8.23 ± 0.07	0.99 ± 0.07	0.01%
Halo	-7.57 ± 0.11	0.94 ± 0.12	-5.17 ± 0.16	0.45 ± 0.16	-7.34 ± 0.16	1.3 ± 0.16	1.72%
				2MASS J			
Disc	-9.9 ± 0.06	1.1 ± 0.05	-10.46 ± 0.06	0.27 ± 0.06	-9.77 ± 0.07	1.12 ± 0.07	0.17%
Halo	-8.09 ± 0.16	0.97 ± 0.09	-7.4 ± 0.11	0.35 ± 0.15	-8.36 ± 0.09	0.88 ± 0.09	9.24%

Notes. $^{(a)}P$ is the probability from the F-test. If the P value is low (e.g. 5%), we can conclude that the double-Gaussian model is statistically significantly better than the single-Gaussian model.

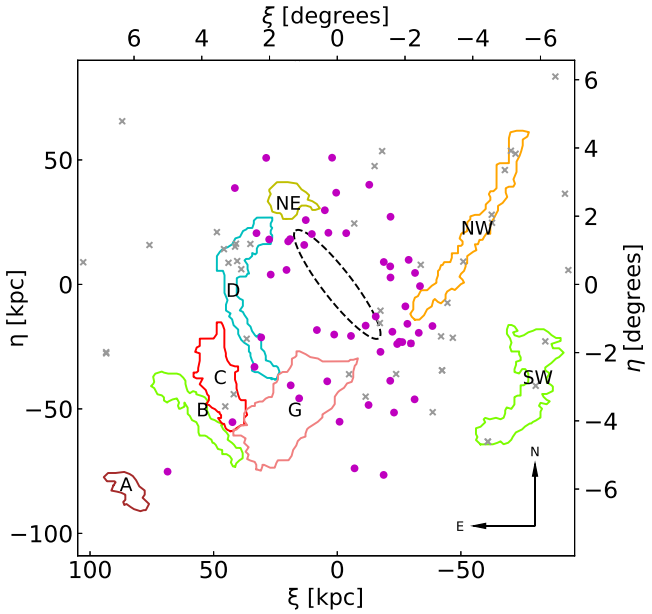

Fig. 13. Location of the GCs and major substructures in the M 31 halo. The filled circles represent the outer-halo GCs with parameter estimates in our study, while the crosses represent the outer-halo GCs without parameter estimates. The types of substructures are A: stream A, B: stream B, C: stream C, D: eastern arc (Stream D), G: giant stream, NE: NE structure, NW: NW stream, and SW: SW cloud. The contours of these substructures are from Fig. 3 of Mackey et al. (2010). The dashed ellipse has a semimajor axis of 2° (27 kpc) representing a disc.

intermediate metallicity ($-1.5 \geq$ [Fe/H] < -0.4) and one metal-poor group ([Fe/H] < -1.5). The masses of disc GCs span a wider range than halo GCs, both in the lower and upper end. The cluster G001 is the most massive one among the halo GCs, and it is also one of the most massive GCs in M 31. It is likely the remnant core of a dwarf galaxy that has lost most of its envelope through tidal interactions with M 31 (Meylan & Heggie 1997; Meylan et al. 2001; Ma et al. 2007a).

4.4. Comparison with the Galactic GC system

Differences between the MW and M 31 GC systems have been reported: (1) M 31 contains more than twice the total number of GCs in the MW (Galleti et al. 2004; Peacock et al. 2010; Caldwell & Romanowsky 2016); (2) the metallicity distribution of the MW GCs is bimodal, with peaks at [Fe/H] ≈ -1.5 and -0.6 dex (Zinn 1985), while that of M 31 GCs includes three components, covering [Fe/H] from -3 to 0.5 (Elson & Walterbos 1988; Caldwell & Romanowsky 2016); and (3) M 31 has a subcomponent of GCs (mostly metal-rich) that closely follow the thin-disc kinematics (e.g. rotation, velocity dispersion), and such a GC system has not yet been found in the MW (Morrison et al. 2004; Caldwell & Romanowsky 2016).

However, there are also remarkable similarities in the chemodynamical properties between the M 31 and MW GC systems. Both of the GC systems are dominated by the metal-poor group, which is spherically distributed and has a high velocity dispersion (Caldwell & Romanowsky 2016). In addition, there is a planar subgroup of dwarf galaxies in the M 31 (Ibata et al. 2013), and they appear to be rotating in the same direction as the outer halo GCs (Veljanoski et al. 2014). A similar plane has also been found in the MW (Metz et al. 2007; Keller et al. 2012; Pawlowski et al. 2012).

By defining the outer halo with $R_p > 20$ kpc, it is intriguing to see that M 31 has more than 100 outer-halo GCs ($N = 113$), which is approximately six times the number of halo GCs found in the MW ($N = 19$). Considering that the total number of M 31 GCs is approximately three times greater than that of the MW, it seems that M 31 contains too many halo GCs. Figure 16 shows the comparison of metallicity and mass between M 31 and Galactic halo GCs. For the Galactic outer-halo GCs, we obtained the metallicities from Harris (1996) and masses from Pryor & Meylan (1993) and Kimmig et al. (2015). The metallicity of the GCs in M 31 halo spans a wider range than that of GCs in the MW halo; the M 31 halo GCs from Caldwell & Romanowsky (2016) present a similar metallicity range with the Galactic halo GCs, but their number is quite small (≈20). For the MW halo, previous studies have shown that it is very metal poor (Ryan & Norris 1991; Chiba & Beers 2000), with a median metallicity of [Fe/H] $= -1.6$. In contrast, the M 31 halo includes a group with intermediate metallicity ([Fe/H] $= -0.6$) and a metal-rich component with [Fe/H] $= -0.2$ (Mould & Kristian 1986; Bellazzini et al. 2003). The minor axis halo fields of M 31 show a de Vaucouleurs $R^{1/4}$-law density profile (Durrell et al. 2004) and intermediate metallicity ([Fe/H] ≈ -0.5), different from the $R^{-3.5}$ shape of the Galactic metal-poor halo (Chiba & Beers 2000; Ibata et al. 2005). However, using a group of kinematically selected stars, Chapman et al. (2006) showed that the M 31 halo population has [Fe/H] ≈ -1.4 with a dispersion of 0.2 dex, very similar to that found in the MW; this indicates the metal-rich component does not have halo-like kinematics (Ibata et al. 2007). These GCs with [Fe/H] > -1 are consistent with the previously discovered

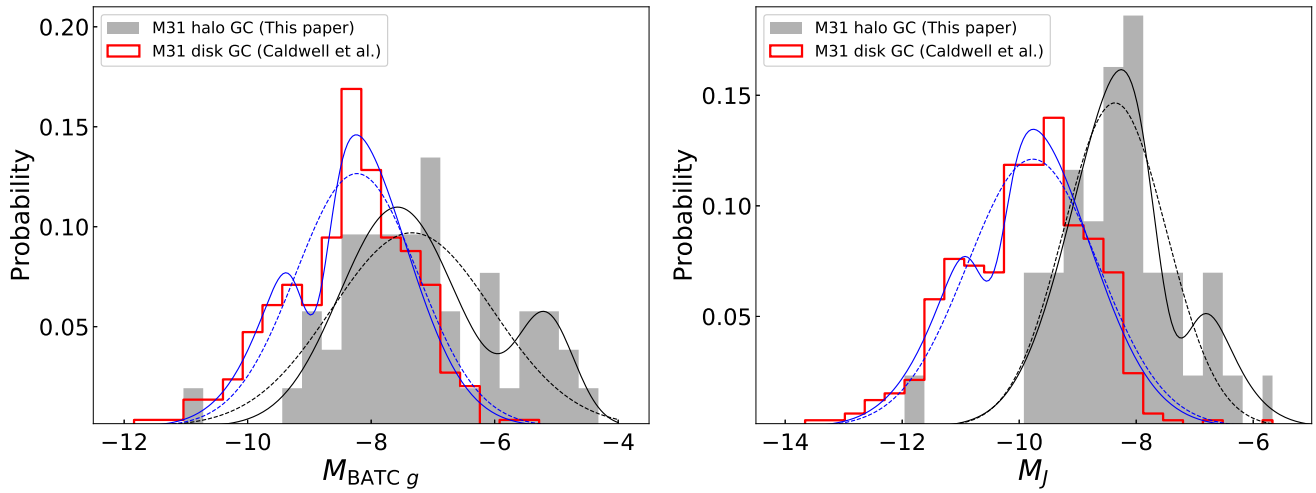

Fig. 14. *Left Panel*: luminosity functions of M 31 disc and halo GCs, using the BATC g magnitudes. The solid blue and black lines are the double-Gaussian fittings to the disc and halo GCLFs, respectively; the dashed blue and black lines are the single-Gaussian fittings to the disc and halo GCLFs, respectively. *Right panel*: luminosity functions of M 31 disc and halo GCs, using the 2MASS J magnitudes.

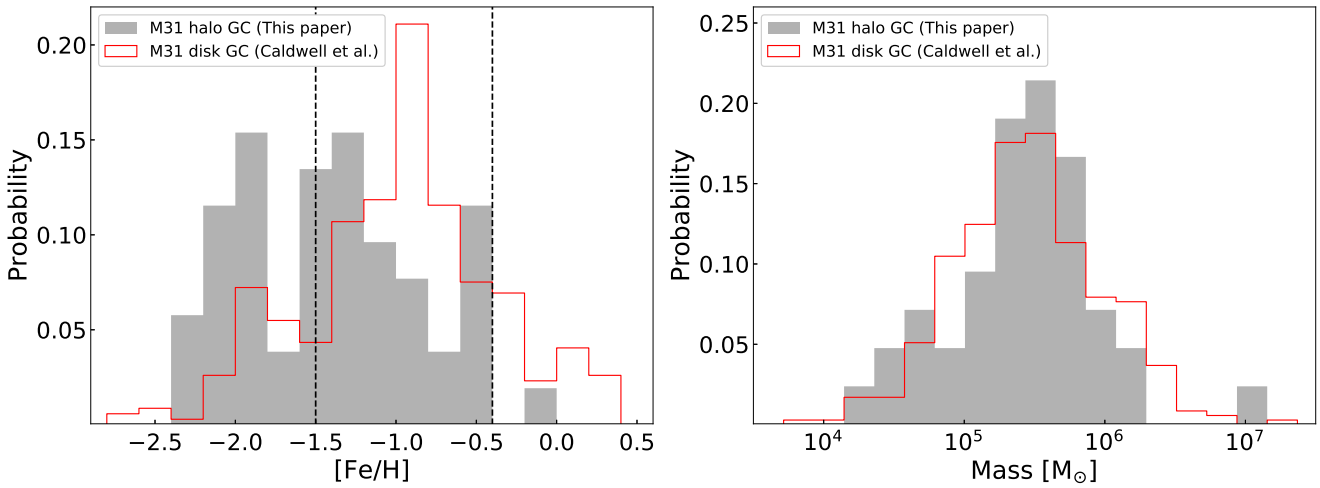

Fig. 15. Comparison of the metallicities (*left panel*) and masses (*right panel*) between the M 31 halo and disc GCs.

component with intermediate metallicities. The host systems of these GCs may have undergone efficient star formation and chemical enrichment, indicating that they were accreted into the M 31 halo at late times (Mackey et al. 2018). All of these are suggestive of an active merger history of M 31 during the formation of the halo (Ibata et al. 2005).

5. Summary

Previous studies have shown that the MW has undergone a small amount of merging, whereas the history of M 31 appears to be very different (e.g. Hammer et al. 2007). This is consistent with the unusual features (e.g. young stellar population, rotational signature of substructures) observed in the M 31 outer regions (Ferguson et al. 2002; Ibata et al. 2005; Richardson et al. 2008), which are thought to be evidence of a history with recent merging (McConnachie et al. 2009). Similarly, the M 31 outer halo GC system shows a strong rotation around the minor optical axis of M 31 (Veljanoski et al. 2014), while the Galactic halo GC population exhibits only slight net rotation (e.g. Brodie & Strader 2006; Deason et al. 2011). Stellar population studies of halo GCs may provide more direct evidence of merger and/or accretion events.

In this paper, we present metallicities, ages, and masses for 53 GCs in the M 31 outer halo, determined by comparing the multicolour photometry with theoretical SSP models. The multicolour photometric data are obtained from the GALEX FUV and NUV, SDSS *ugriz*, 15 intermediate-band filters of BATC, and 2MASS JHK_s, which constitute the SEDs covering 1538–20 000 Å. In general, our results based on SED fitting are consistent with previous studies.

We studied the spatial distribution of the halo GCs, and found no clear trend of metallicity and mass with the de-projected radius. We also found that the halo GCs with age younger than ~8 Gyr are mostly located at the de-projected radii around 100 kpc, but this may be due to a selection effect; and that most metal-poor GCs ([Fe/H] < −1.5) have an age of 14 Gyr. Our results show that there is an extended feature towards M 33 for these metal-poor GCs, which is along the direction of the M 31 minor optical axis, consisting of four GCs: H22, H27, HEC11, and HEC13. However, the feature is likely a consequence of our unevenly pointed observations. In our sample, there are eight GCs showing spatial coincidence with these halo substructures, and these GCs have consistent metallicities with their spatially associated substructures. Together with

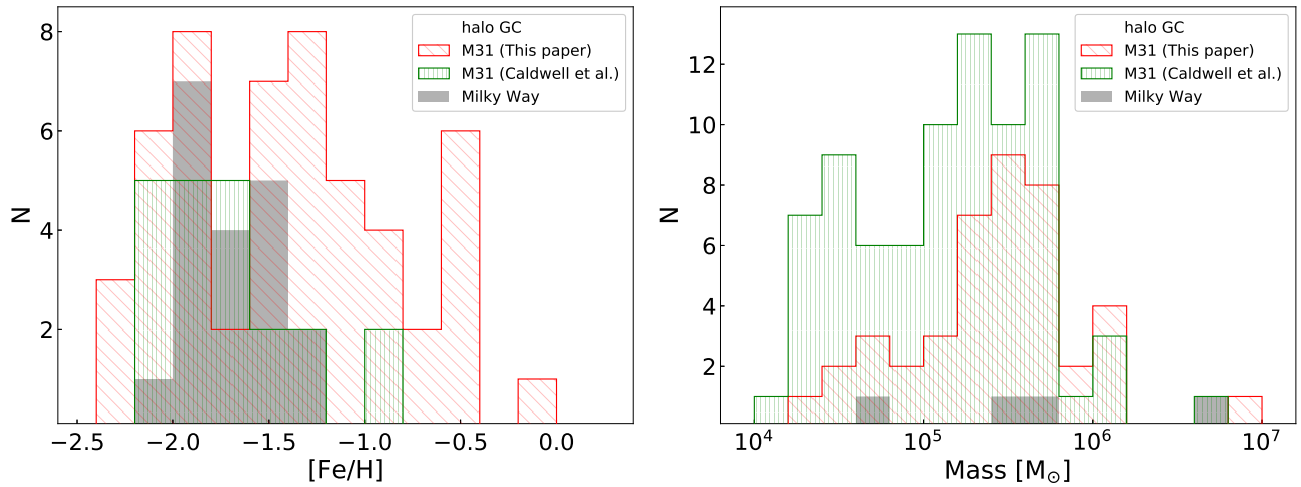

Fig. 16. Comparison of the metallicities (*left panel*) and masses (*right panel*) between the M 31 and Galactic halo GCs.

the dynamical link between the halo GCs and the substructures found in previous kinematic analyses, our results provide further evidence of the physical association between them.

Our results show that both the disc and halo GCs in M 31 show a bimodal luminosity distribution, and that there are many more faint GCs in the halo than in the disc, the former contributing to the fainter part in the halo GCLF. Because most of the GCs in the outer halo of M 31 were accreted from dwarf galaxies, this bimodality of the GCLF may reflect a different origin or evolution environment for these halo GCs. The M 31 disc GCs include three metallicity components, covering −3–0.5, while there are only two groups for the outer halo GCs – one group with intermediate metallicity ($-1.5 \geq$ [Fe/H] < -0.4) and one metal-poor group ([Fe/H] < -1.5).

The total number of GCs in M 31 is approximately three times greater than in the MW, however M 31 has more than 100 outer-halo GCs ($N = 113$), which is approximately six times the number of halo GCs in the MW ($N = 19$). It seems that M 31 contains too many halo GCs. The metallicity of the GCs in the halo of M 31 spans a wider range than that of the GCs in the MW halo, since the Galactic halo GCs are mostly metal-poor. Both the numerous halo GCs and the higher-metallicity component are suggestive of an active merger history of M 31 during halo formation.

Acknowledgements. We especially thank the anonymous referee for his/her thorough report and helpful comments and suggestions, which significantly improved the paper. We thank Dr. Zhou Fan for helpful discussions. This work was supported by the Chinese National Natural Science Foundation grant Nos. 11603035, 11873053, 11433005, 11273028, 11333004, 2016YFA0400800, and 11425313.

References

Agar, J. R. R., & Barmby, P. 2013, AJ, 146, 135
Alves-Brito, A., Forbes, D. A., Mendel, J. T., Hau, G. K. T., & Murphy, M. T. 2009, MNRAS, 395, L34
Anders, P., Bissantz, N., Fritze-v. Alvensleben, U., & de Grijs, R. 2004, MNRAS, 347, 196
Barmby, P., Huchra, J. P., Brodie, J. P., et al. 2000, AJ, 119, 727
Barmby, P., McLaughlin, D. E., Harris, W. E., Harris, G. L. H., & Forbes, D. A. 2007, AJ, 133, 2764
Bellazzini, M., Cacciari, C., Federici, L., Fusi Pecci, F., & Rich, M. 2003, A&A, 405, 867
Bertelli, G., Bressan, A., Chiosi, C., Fagotto, F., & Nasi, E. 1994, A&AS, 106, 275
Bertin, E., & Arnouts, S. 1996, A&AS, 117, 393
Brodie, J. P., & Strader, J. 2006, ARA&A, 44, 193
Bruzual, G., & Charlot, S. 2003, MNRAS, 344, 1000
Caldwell, N., & Romanowsky, A. J. 2016, ApJ, 824, 42
Caldwell, N., Harding, P., Morrison, H., et al. 2009, AJ, 137, 94
Caldwell, N., Schiavon, R., Morrison, H., Rose, J. A., & Harding, P. 2011, AJ, 141, 61
Cardelli, J. A., Clayton, G. C., & Mathis, J. S. 1989, ApJ, 345, 245
Chapman, S. C., Ibata, R., Lewis, G. F., et al. 2006, ApJ, 653, 255
Chen, B., Liu, X., Xiang, M., et al. 2016, AJ, 152, 45
Chiba, M., & Beers, T. C. 2000, AJ, 119, 2843
Colucci, J. E., Bernstein, R. A., & Cohen, J. G. 2014, ApJ, 797, 116
Côté, P., Marzke, R. O., West, M. J., & Minniti, D. 2000, ApJ, 533, 869
Da Costa, G. S., & Armandroff, T. E. 1995, AJ, 109, 2533
Deason, A. J., Belokurov, V., & Evans, N. W. 2011, MNRAS, 411, 1480
de Grijs, R., Fritze-v. Alvensleben, U., & Anders, P. 2003, MNRAS, 342, 259
de Jong, R. S. 1996, A&A, 313, 377
di Tullio Zinn, G., & Zinn, R. 2013, AJ, 145, 50
di Tullio Zinn, G., & Zinn, R. 2014, AJ, 147, 90
Durrell, P. R., Harris, W. E., & Pritchet, C. J. 2004, AJ, 128, 260
Elson, R. A., & Walterbos, R. A. M. 1988, ApJ, 333, 594
Fan, Z., & Wang, S. 2017, Ap&SS, 362, 193
Fan, X., Burstein, D., Chen, J.-S., et al. 1996, AJ, 112, 628
Fan, Z., Ma, J., de Grijs, R., & Zhou, X. 2008, MNRAS, 385, 1973
Fan, Z., Ma, J., & Zhou, X. 2009, Res. Astron. Astrophys., 9, 993
Fan, Z., de Grijs, R., & Zhou, X. 2010a, ApJ, 725, 200
Fan, Z., Ma, J., Zhou, X., & Jiang, Z. 2010b, PASP, 122, 636
Ferguson, A. M. N., Irwin, M. J., Ibata, R. A., Lewis, G. F., & Tanvir, N. R. 2002, AJ, 124, 1452
Galleti, S., Federici, L., Bellazzini, M., Fusi Pecci, F., & Macrina, S. 2004, A&A, 416, 917
Hammer, F., Puech, M., Chemin, L., Flores, H., & Lehnert, M. D. 2007, ApJ, 662, 322
Harris, W. E. 1996, AJ, 112, 1487
Harris, W. E., Ciccone, S. M., Eadie, G. M., et al. 2017, ApJ, 835, 101
Huchra, J. P., Brodie, J. P., & Kent, S. M. 1991, ApJ, 370, 495
Huxor, A. P., Tanvir, N. R., Ferguson, A. M. N., et al. 2008, MNRAS, 385, 1989
Huxor, A. P., Ferguson, A. M. N., Tanvir, N. R., et al. 2011, MNRAS, 414, 770
Huxor, A. P., Mackey, A. D., Ferguson, A. M. N., et al. 2014, MNRAS, 442, 2165
Ibata, R. A., Gilmore, G., & Irwin, M. J. 1994, A&A, 370, 194
Ibata, R., Irwin, M., Lewis, G., Ferguson, A. M. N., & Tanvir, N. 2001, A&A, 412, 49
Ibata, R., Chapman, S., Ferguson, A. M. N., et al. 2005, ApJ, 634, 287
Ibata, R., Martin, N. F., Irwin, M., et al. 2007, ApJ, 671, 1591
Ibata, R. A., Lewis, G. F., Conn, A. R., et al. 2013, A&A, 493, A62
Ibata, R. A., Lewis, G. F., McConnachie, A. W., et al. 2014, ApJ, 780, 128
Kang, Y., Rey, S.-C., Bianchi, L., et al. 2012, ApJS, 199, 37
Kaviraj, S., Rey, S.-C., Rich, R. M., Yoon, S.-J., & Yi, S. K. 2007, MNRAS, 381, L74
Keller, S. C., Mackey, D., & Da Costa, G. S. 2012, ApJ, 744, 57
Kent, S. 1989, AJ, 97, 1614
Kimmig, B., Seth, A., Ivans, I. I., et al. 2015, AJ, 149, 53

Ma, J., de Grijs, R., Chen, D., et al. 2007a, MNRAS, 376, 1621
Ma, J., Yang, Y., Burstein, D., et al. 2007b, ApJ, 659, 359
Ma, J., Fan, Z., de Grijs, R., et al. 2009, AJ, 137, 4884
Ma, J., Wang, S., Wu, Z., et al. 2012, AJ, 143, 29
Ma, J., Wang, S., Wu, Z., et al. 2015, AJ, 149, 56
Mackey, A. D., Huxor, A., Ferguson, A. M. N., et al. 2006, ApJ, 653, L105
Mackey, A. D., Huxor, A., Ferguson, A. M. N., et al. 2007, ApJ, 655, L85
Mackey, A. D., Huxor, A. P., Ferguson, A. M. N., et al. 2010, ApJ, 717, L11
Mackey, D., Ferguson, A., & Huxor, A. 2018, MNRAS, submitted [arXiv:1810.10719]
Martin, N. F., Ibata, R. A., Bellazzini, M., et al. 2004, MNRAS, 348, 12
Mateu, C., Vivas, A. K., Zinn, R., Miller, L. R., & Abad, C. 2009, AJ, 137, 4412
McConnachie, A. W., Irwin, M. J., Ferguson, A. M. N., et al. 2005, MNRAS, 356, 979
McConnachie, A. W., Irwin, M. J., Ibata, R. A., et al. 2009, A&A, 461, 66
McConnachie, A. W., Ibata, R., Martin, N., et al. 2018, ApJ, 868, 55
Metz, M., Kroupa, P., & Jerjen, H. 2007, MNRAS, 374, 1125
Meylan, G., & Heggie, D. C. 1997, A&ARv, 8, 1
Meylan, G., Sarajedini, A., Jablonka, P., et al. 2001, AJ, 122, 830
Morrison, H. L., Harding, P., Perrett, K., & Hurley-Keller, D. 2004, ApJ, 603, 87
Mould, J., & Kristian, J. 1986, ApJ, 305, 591
Nantais, J. B., Huchra, J. P., Barmby, P., Olsen, K. A. G., & Jarrett, T. H. 2006, AJ, 131, 1416
Pawlowski, M. S., Pflamm-Altenburg, J., & Kroupa, P. 2012, MNRAS, 423, 1109
Peacock, M. B., Maccarone, T. J., Knigge, C., et al. 2010, MNRAS, 402, 803
Peacock, M. B., Zepf, S. E., Maccarone, T. J., & Kundu, A. 2011, ApJ, 737, 5
Peng, E. W., Jordán, A., Côté, P., et al. 2006, ApJ, 639, 95
Perrett, K. M., Bridges, T. J., Hanes, D. A., et al. 2002, AJ, 123, 2490
Pryor, C., & Meylan, G. 1993, Structure and Dynamics of Globular Clusters, 50, 357
Puzia, T. H., Perrett, K. M., & Bridges, T. J. 2005, A&A, 434, 909
Rich, R. M., Corsi, C. E., Cacciari, C., et al. 2005, AJ, 129, 2670
Richardson, J. C., Ferguson, A. M. N., Johnson, R. A., et al. 2008, AJ, 135, 1998
Ryan, S. G., & Norris, J. E. 1991, AJ, 101, 1865
Sakari, C. M., Venn, K. A., Mackey, D., et al. 2015, MNRAS, 448, 1314
Salpeter, E. E. 1955, ApJ, 121, 161
Schlafly, E. F., & Finkbeiner, D. P. 2011, ApJ, 737, 103
Stetson, P. B. 1987, PASP, 99, 191
Veljanoski, J., Mackey, A. D., Ferguson, A. M. N., et al. 2014, MNRAS, 442, 2929
Wang, S., Fan, Z., Ma, J., de Grijs, R., & Zhou, X. 2010, AJ, 139, 1438
Wang, S., Ma, J., Wu, Z., & Zhou, X. 2014, AJ, 148, 4
White, S. D. M., & Rees, M. J. 1978, MNRAS, 183, 341
Zheng, Z., Shang, Z., Su, H., et al. 1999, AJ, 117, 2757
Zinn, R. 1985, ApJ, 293, 424
Zucker, D. B., Kniazev, A. Y., Bell, E. F., et al. 2004, ApJ, 612, L117